# Supplementary Information: Spin resonance linewidths of bismuth donors in silicon coupled to planar microresonators

James O'Sullivan,[1,*] Oscar W. Kennedy,[1,*] Christoph W. Zollitsch,[1] Mantas Šimėnas,[1] Christopher N. Thomas,[2] Leonid V. Abdurakhimov,[1,†] Stafford Withington,[2] and John J. L. Morton[1,3,‡]

[1] *London Centre for Nanotechnology, UCL, 17-19 Gordon Street, London, WC1H 0AH, UK*
[2] *Cavendish Laboratory, University of Cambridge, JJ Thomson Ave, Cambridge CB3 0HE, UK*
[3] *Department of Electrical and Electronic Engineering, UCL, Malet Place, London, WC1E 7JE, UK*

### A. The bismuth donor spin system

The Bi:Si spin Hamiltonian results, under the application of a magnetic field, in 20 non-degenerate energy levels, as shown in the Breit-Rabi diagram in Fig. S1. At low fields, we label the eigenstates by the total spin **F** and its projection onto the $z$ axis $m_F$.

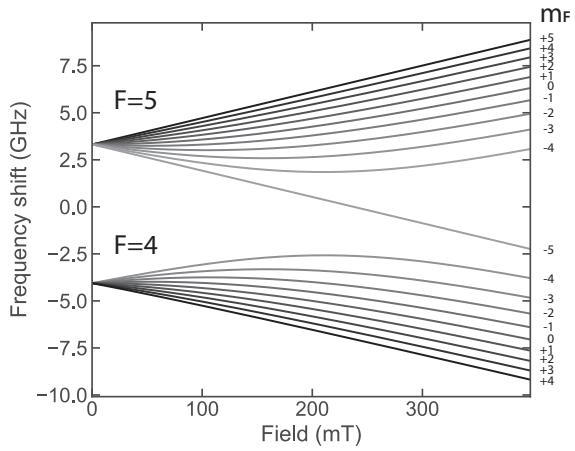


Figure S1. Breit-Rabi diagram of Bi:Si spin system. At fields below ∼100 mT, the hyperfine interaction dominates, hence we label states by their total spin state $F$ and its projection on the $z$ axis $m_F$. Although from $100 - 400$ mT we are in a regime where the Zeeman and hyperfine interactions are similar in strength, we will continue to use the low field quantum numbers **F** and $m_F$ for simplicity.

We now wish to find the relative transition strengths (given by the transition rates) between any two eigenstates under the influence of an arbitrary drive field $B_1$. To first order, the transition rate $\Gamma$ from one initial state $|\, i\rangle$ into a continuum of final states $|\, f\rangle$ with a density of final states $\rho$ of a system under the influence of a perturbing Hamiltonian $H$ is governed by Fermi's Golden Rule (FGR):

$$\Gamma = \frac{2\pi}{\hbar} \left|\langle\, f|\, H|\, i\rangle\right|^2 \rho. \tag{1}$$

In this case we have a single discrete final state, thus the density of states can be considered to be a delta function at the frequency of the transition. As we are interested only in the relative transition rates we can discard all constants and use a normalised field vector $\hat{\mathbf{B}}$ as the perturbing field:

$$\Gamma \propto \left|\left\langle\, f\right|\, \hat{\mathbf{B}} \cdot \mathbf{S} \left|\, i\right\rangle\right|^2. \tag{2}$$

This allows us to determine the relative transition strengths and predicts two types of transition, $S_{\mathrm{x}}$ and $S_{\mathrm{z}}$, corresponding to $\hat{\mathbf{B}} = (1,0,0)$ and $\hat{\mathbf{B}} = (0,0,1)$, respectively.

### B. Measurement Setup and device fabrication and characterization

The resonators were patterned onto the Bi implanted Si using a lift-off process. For this process, the Si was diced into 13.5 mm × 7.5 mm chips for compatibility with tooling. Several device chips were fabricated simultaneously on each of the larger host chips. The photoresist stencil was formed by an image reversal process using optical contact lithography. This process was optimized to give an undercut resist profile, which helps to eliminate fence formation at the film edges on lift-off. The 100 nm of niobium was deposited by DC sputtering in a system with a base pressure of $5 \times 10^{-10}$ mTorr. Sputtering power was 129 W and Ar pressure 3.4 mTorr. Deposition time to give 100 nm was determined by calibration. The deposition conditions had been optimized previously to give a film with low intrinsic stress on Si-like substrates. For 100 nm niobium thick films deposited in this way, we typically measure a resistivity of 8.8 μΩcm at 20 K and superconducting transition temperature in the range 8-9 K.

To characterize the microresonators we measure $S_{21}$ transmission through a copper box which is modulated by the microresonator. We fit the modulation (in linear magnitude) with a Breit-Wigner-Fano function:

$$S_{21\mathrm{Lin}}(f) = K\frac{q\kappa + f - f_0}{\kappa^2 + (f - f_0)^2} + mx + c \tag{3}$$

* These authors have contributed equally to this work
† Present address: NTT Basic Research Laboratories, NTT Corporation, 3-1 Morinosato-Wakamiya, Atsugi, Kanagawa 243-0198, Japan
‡ jjl.morton@ucl.ac.uk

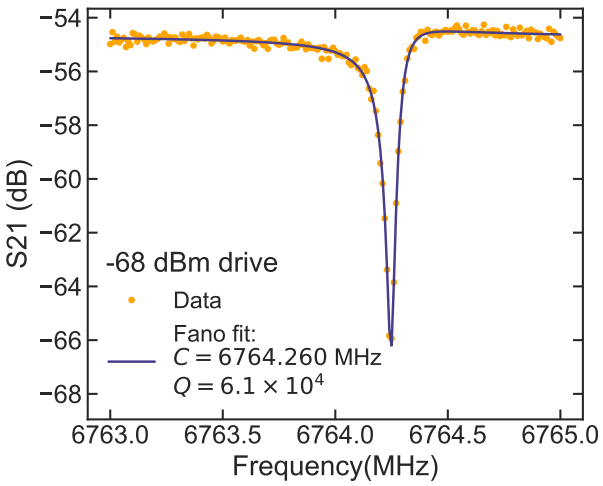


Figure S2. $S_{21}$ measurement of a resonator at -68 dBm at the antenna of the copper box. Data (yellow) is overlaid by a fit to Eqn. 3 of the SI (blue) giving a resonator frequency of 6764.260 MHz and Q-factor of $6.1\times10^4$. The excellent fit to theory means that the fit precisely overlays the data in the centre of the resonance.

where $K$ determines the size of the modulation, $q$ is an asymmetry parameter, $f_0$ is the central frequency of the resonator, $\kappa$ is the HWHM of the resonator and the $mx+c$ term is an approximation to the background transmission. The Fano resonance lineshape arises as a result of interference of microwave signals travelling directly from the input antenna to the recieve antenna with the signal absorbed and remitted by the resonator. In the limit of zero direct transmission between the antennae, this function reduces to a Lorentzian, which is the underlying true resonance lineshape. This function fits our resonance notch well and an example is shown in Fig. S2.

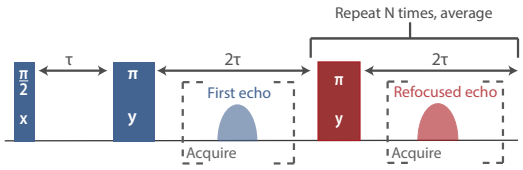


Figure S3. Schematic of the CPMG averaging scheme. After the initial excitation and refocusing pulses, spaced by time $\tau$, a train of $N$ refocusing pulses is applied after the first echo with spacing $2\tau$, generating a train of echoes. These are all acquired in a single shot and averaged.

A technique for reducing measurement time, shown in Fig. S3, was employed for Hahn echo detection for these measurements. After the Hahn echo has been measured, it is possible to refocus the spin system again to form another echo using a CPMG pulse sequence [1, 2], provided the coherence time and $T_1$ relaxation time is sufficiently long. This is because only a small fraction of the energy

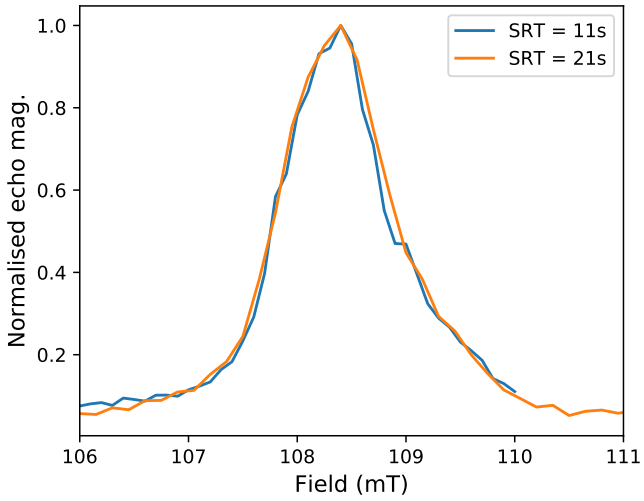


Figure S4. Normalised CPMG EDFS collected at 11s and 21s SRT showing no dependence of the linshape on SRT.

stored in the spins is emitted during a Hahn echo. It has been shown by Mentink-Vigier et al. that such pulse sequences could be used for the purposes of averaging to improve ESR sensitivity [3]. In these measurements the $\pi/2$ ($\pi$) pulses were 2 µs (4 µs) and $\tau$ = 60 µs. In field sweeps, typically the field step results in a frequency shift greater than the resonator bandwidth and take ∼30 s for each field step which dominates the shot repetition time (SRT). Extensive tests show that, as expected, lineshapes taken with CPMG acquisitions are insensitive to SRT as shown, for example, in Fig. S4.

The full measurement setup is shown in Fig. S5. An arbitrary wave-form generator (AWG) is used to send pulse sequences to a vector signal generator (VSG) which is set to the frequency of the superconducting resonator as determined by fitting to a VNA transmission measurement of the resonator. The pulse emitted from the VSG is amplified using a 30dB solid state amplifier with max output power +35 dBm before passing through cryogenic attenuators (30 dB in total) to thermalise the centre conductor of the input line and attenuate room temperature noise. Fast microwave switches gate the signal from the pulse amplifier when pulses are not being sent to ensure amplified room temperature noise is not sent into the fridge. The signal from the receive antenna inside the copper box is sent via two circulators to a Josephson Parametric Amplifier (JPA) which amplifies the signal in reflection. The amplifier is driven via a directional coupler by a dedicated microwave source. The JPA has typical gain of 10 dB although this varies depending on the settings of the JPA which is optimized for signal to noise ratio, rather than absolute gain. The signal is further amplifed by ∼40 dB at 4 K by a high electron mobility transistor (HEMT) and again by ∼40dB at room temperature before being mixed down in frequency by an IQ mixer. The IQ mixer uses a local oscillator (LO) produced by

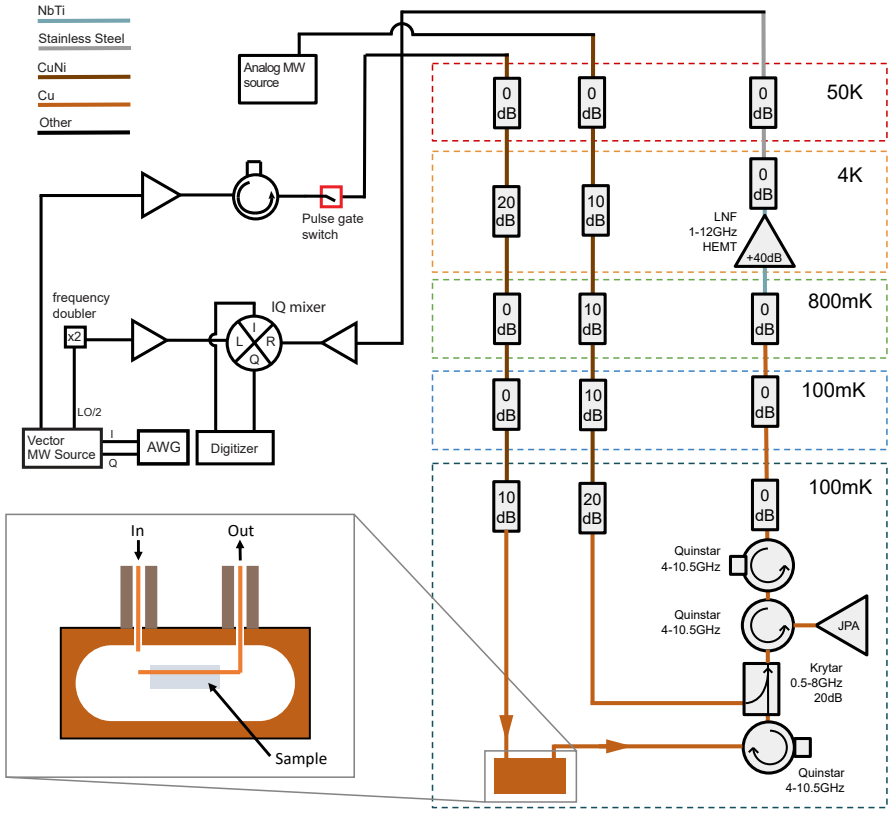


Figure S5. Schematic of the spectrometer and dilution fridge setup. The copper box housing the resonator is magnified to show the configuration of the sample and antennae inside. The receive antenna is considerably longer than the input antenna to increase coupling to the resonator and maximise signal. Coaxial cable types inside the fridge have been colour coded.

the VSG to mix down the signal. The VSG outputs a reference signal at half the VSG signal frequency and so a frequency doubler is used to produce a LO at the correct frequency which is amplified by 20dB to produce a signal with sufficient power for the IQ mixer. The mixed down signal is detected using a digitiser.

### C. Nearest neighbour mass fit

To fit echo detected field sweeps (EDFS) we consider the shifts to hyperfine constant due to the average mass of the bismuth donor's nearest neighbour silicon atoms. Using the isotopic abundance of natural silicon, we calculate a trinomial distribution to determine the probability of the different nearest neighbour configurations. At $\partial f/\partial A = 5$, as all of these transitions are up to a few %, the shift is 1.7 MHz/$\Delta M_{\mathrm{NN}}$ where $\Delta M_{\mathrm{NN}}$ is the difference between the nuclear mass of all four nearest neighbour Si atoms and four $^{28}$Si. This means we know both the fraction of bismuth donors in each configuration and the relative frequency of donors in each configuration. We define a series of Gaussians with a common width and with relative amplitude determined by the fraction of bismuth donors in the configuration and relative frequency based on $\Delta M_{\mathrm{NN}}$ for the configuration. For $S_{\mathrm{x}}$ transitions where transitions are quasi-degenerate we consider the two transitions, calculating an offset frequency from the spin Hamiltonian and relative amplitudes from the matrix element in FGR as shown in Fig. S6.

We then fit the EDFS to the series of Gaussians with two free parameters, the common width of the Gaussians and a correction to the field where the $\Delta M_{\mathrm{NN}} = 0$ line intersects with the resonator to allow for small field miscalibrations which are always $< 1\%$. This results in fits which accurately capture the lineshape such as that shown in Fig. 3(a) in the main text. A tail at high frequency (which for the transition with negative $\partial f/\partial B$ shown in Fig. 3(a) is at high field) which is badly captured by the fit routine is common to many transitions but more clearly resolved for transitions with low $|\partial f/\partial B|$. This may indicate some regions of high strain.

### D. Clock transition measurements with 3D cavity

Bismuth donors are measured at a clock transition using a 3D cavity. This means that no planar devices with

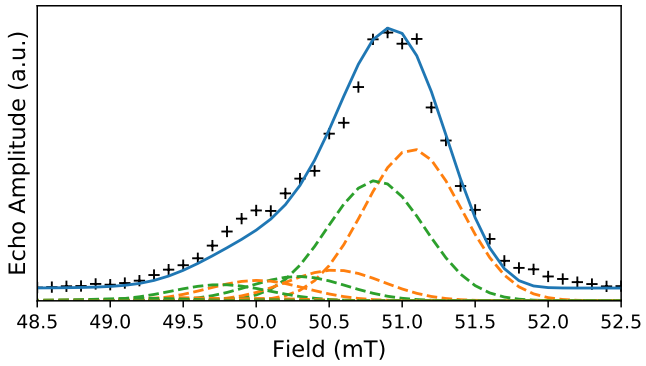


Figure S6. A fit to an EDFS of an $S_x$ transition considering nearest neighbour mass shifts and quasi-degenerate transitions. The peaks from the two transitions are shown in green and orange, with relative amplitude determined by the FGR matrix element. The total fit is shown in blue and data as black crosses.

mismatched CTE are present on top of the host Si and thus it remains unstrained. Using the same loop-gap copper resonator as that used in Ref. 4 we measure an EDFS at the 7.38 GHz clock transition. Due to the small number of spins in a thin implanted layer we use a modified ESR probe with an in-built cryogenic HEMT amplifier described in a forthcoming publication. The results of this are shown in Fig. S7.

In Fig. S7(a) we show the echoes in the time domain as the field is stepped across the clock transition in 1 mT steps. Integrating the centre of the echo magnitude as indicated by the dashed black lines in Fig. S7(a) we obtain an EDFS shown in Fig. S7(b). The dip at the centre of the clock transition is caused by the ∼10 % of bismuth donors with nearest neighbour mass shifts of 3.4 MHz (i.e. $\Delta M_{\mathrm{NN}} = 2$) dropping out of the bandwidth of the cavity. Performing the fast fourier transform (FFT) of the echoes shown in Fig. S7(a) allows us to resolve the spectrum of the bismuth. The parabolic dispersion of the most intense peak which is due to all nearest neighbour silicon atoms being $^{28}$Si is clearly seen. These peaks are fit by a Gaussian shown in red at the bottom of the clock transition and their width is shown in Fig. S7(d). In addition to the peaks arising from nearest neighbours all being $^{28}$Si we can resolve peaks arising from $\Delta M_{\mathrm{NN}} = 1, 2$. These peaks are weaker but follow the same quadratic dispersion at the bottom of the clock transition. We extract the minimum linewidth of the bismuth donors by taking the HWHM of the Gaussin which fits the FFT in Fig. S7(c) and show linewidth is minimized at ∼0.5 MHz.

### E. Resonator and strain simulations

Resonators are simulated using COMSOL ™ with simulations of the magnetic field distribution about the resonator and strain induced by differences in coefficients in thermal expansion solved together.

The magnetic field about the resonator is determined following Refs. [5, 6]. The integrated current due to zero point fluctuations (ZPF), $\delta i = 2\pi f\sqrt{\hbar/2Z}$ where $Z$ is the impedance of the resonator. The impedance is determined assuming a lumped element geometry where $Z = \sqrt{L/C}$ and $f = 2\pi\sqrt{1/LC}$. The capacitance of the capacitative arms is determined using a coplanar capacitance calculator, the resonator frequency is measured and thus the impedance is determined to be ∼100 Ω. The current fluctuations can then be analytically determined given the penetration depth of niobium being ∼50 nm [7].

As described in the main text we calculate a spatially varying contribution factor from the driven microwave field $B_{1,\mathrm{driven}} = B_1 A_{\mathrm{pulse}}$ at each pixel in the FE simulation. This is shown for $S_z$ transitions in Fig. S8 for different powers of initial pulse. At high powers banding occurs where spins in consecutive bands provide opposite contributions.

Considering how strain shifts the hyperfine frequency, we can simulate an expected EDFS as is shown in Fig. S10. This is achieved by solving the spin Hamiltonian for a number of different hyperfine constants. We then sum a series of Gaussians, one for each pixel in the FE simulation. The centre of the Gaussian is the frequency which the resonator crosses the transition based on the hyperfine constant at that pixel accounting for strain and mass shifts. The amplitude of the Gaussian is set by the contribution factor at that pixel. All Gaussians are given the same common width of 660 kHz. We do this for a few values of $A_{\mathrm{pulse}}$ and average them to account for inhomogeneities along the inductor wire. We then use the resonator dispersion to convert this frequency spectrum into field, thus simulating the EDFS.

The simulated EDFSs have some broad qualitative agreement to the measured EDFSs. At low powers the line saturates in a broad peak. At high powers there is a peak of approximately the correct width in field. At intermediate powers there are oscillations in intensity within the field sweep. These simulated EDFS do not however accurately reproduce the experimental EDFS. There are many potential candidates for this discrepancy; significant, unaccounted, inhomogeneities along the inductor wire, contribution factors in the CPMG pulse sequence not following the $\sin^3(\theta)$ dependence of Hahn echo, errors in the FE simulation of strain, incorrect values of penetration depth being used to calculate $B_1$ to name a few. The broad qualitative agreement is promising, indicating that we capture the main features of this system. Further work, particularly on the strain simulations, is needed for a good qualitative agreement between simulation and experiment.

We also consider, and rule out, the Meissner effect as the dominant cause of this line broadening. Using COMSOL, we model the resonator as strongly diamagnetic and compute the deformed static field about the resonator. Using this static field to compute the spin Hamiltonian results in EDFS drastically different to experiment and,

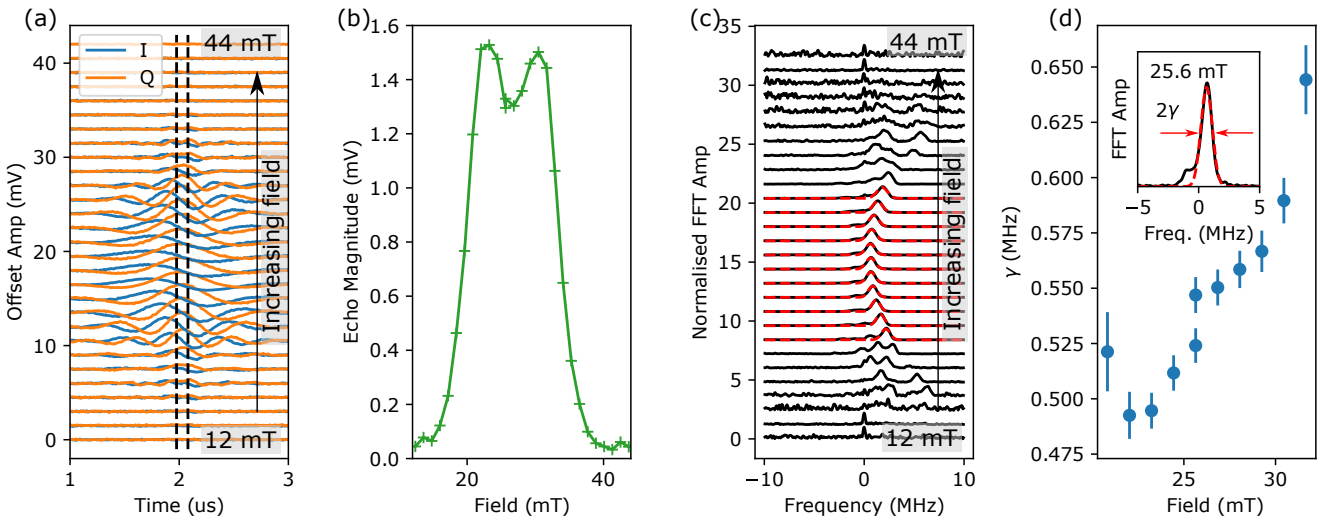


Figure S7. Results of EDFS measurements taken at an $S_x$ transition using a 3D loop-gap copper resonator at 10 K. (a) Raw echo signal quadratures I (blue curves) and Q (orange curves) at different field values swept across the clock transition. Dashed vertical lines correspond to the integration time interval which was used to calculate data shown in Fig.S7(c). (c) Black curves correspond to normalised amplitudes of fast Fourier transform (FFT) of the complex data, $I + j \times Q$, where I and Q are signal components shown in Fig.S7(a).In addition to the dominant peaks, weaker peaks from nearest-neighbour mass shifts are resolved. The clock transition, where dominant peaks reach a minimum in frequency, is clear. Red curves correspond to results of a Gaussian fitting of the dominant peaks at the clock transition. (d) Spin linewidths $\gamma$ (half-width-at-half-maximum, HWHM) extracted from the data shown in Fig.S7(c) using the Gaussian fitting of the dominant peaks. The minimum linewidth value is 0.5 MHz. The inset shows an example of fitting results at the centre of the clock transition (also shown in Fig.S7(c))

most pertinently, means that at low powers the simulated peak position, which is already too low in field, shifts further downwards in field. These low power spectra, arising from spins closest to the resonator, are where this effect should be strongest and given that the incorrect sign of the effect, we conclude is not the dominant broadening process.

### F. Cooperativity and strong coupling in the small $\kappa$ limit

The expression for cooperativity, $C = g_{\text{ens}}^2/\kappa\gamma = g_0^2 N/\kappa\gamma$, is derived from the Tavis-Cummings Hamiltonian considering a cavity coupled to $N$ two-level-systems — in our case, spins. When the spins are inhomogeneously broadened such that the homogeneous linewidth, $\gamma_{\text{h}} = 1/T_2$, is small and we are in the regime $\gamma_{\text{h}} \ll \kappa < \gamma$, as is the case in this paper, these spins can fall outside of the cavity linewidth. The traditional definition of cooperativity indicates that spins outside the bandwidth of the cavity (i.e. no spectral overlap) contribute to the cooperativity.

In the limit $\gamma_{\text{h}} \ll \kappa < \gamma$, it makes more sense to consider only the spins within the resonator bandwidth, such that any change to spins that fall outside the resonator bandwidth cannot affect $C$ or the coupling. We can instead use the coupled spin linewidth $\gamma_{\text{corr}} \equiv \kappa$ and make a correction to the number of spins $N$ in the ensemble to ensure we only count spins within the resonator bandwidth. The corrected spin number is

$$N_{\text{corr}} = N \frac{\int_{-\infty}^{\infty} \frac{\eta}{\eta_{\text{max}}} \rho \, df}{\int_{-\infty}^{\infty} \rho \, df} \tag{4}$$

where $\rho$ is the spin spectral density, $\eta$ is the resonator power spectral density and $\eta_{\text{max}}$ is the maximum value of $\eta$, such that $\eta/\eta_{\text{max}}$ is the dimensionless resonator lineshape, normalised to an amplitude of 1. The term $\rho\eta/\eta_{\text{max}}$ is effectively a corrected spin lineshape that accounts only for spins coupled to the resonator. The ratio of the area of the corrected lineshape to the original lineshape gives the correction factor to $N$. Using this, we can now write the corrected ensemble cooperativity:

$$C_{\text{corr}} = \frac{g_0^2 N_{\text{corr}}}{\kappa^2} \tag{5}$$

Now consider the simple case of a uniformly broadened spin ensemble coupled to a narrow-bandwidth resonator with identical lineshape and with no detuning between the two. In this case the spin spectral density is approximately constant over the bandwidth of the resonator and the corrected spin lineshape takes on exactly the lineshape of the resonator, with the same amplitude as the original spin line. Then $N_{\text{corr}}$ is simply $N$ multiplied by the ratio of the resonator linewidth to the spin ensemble

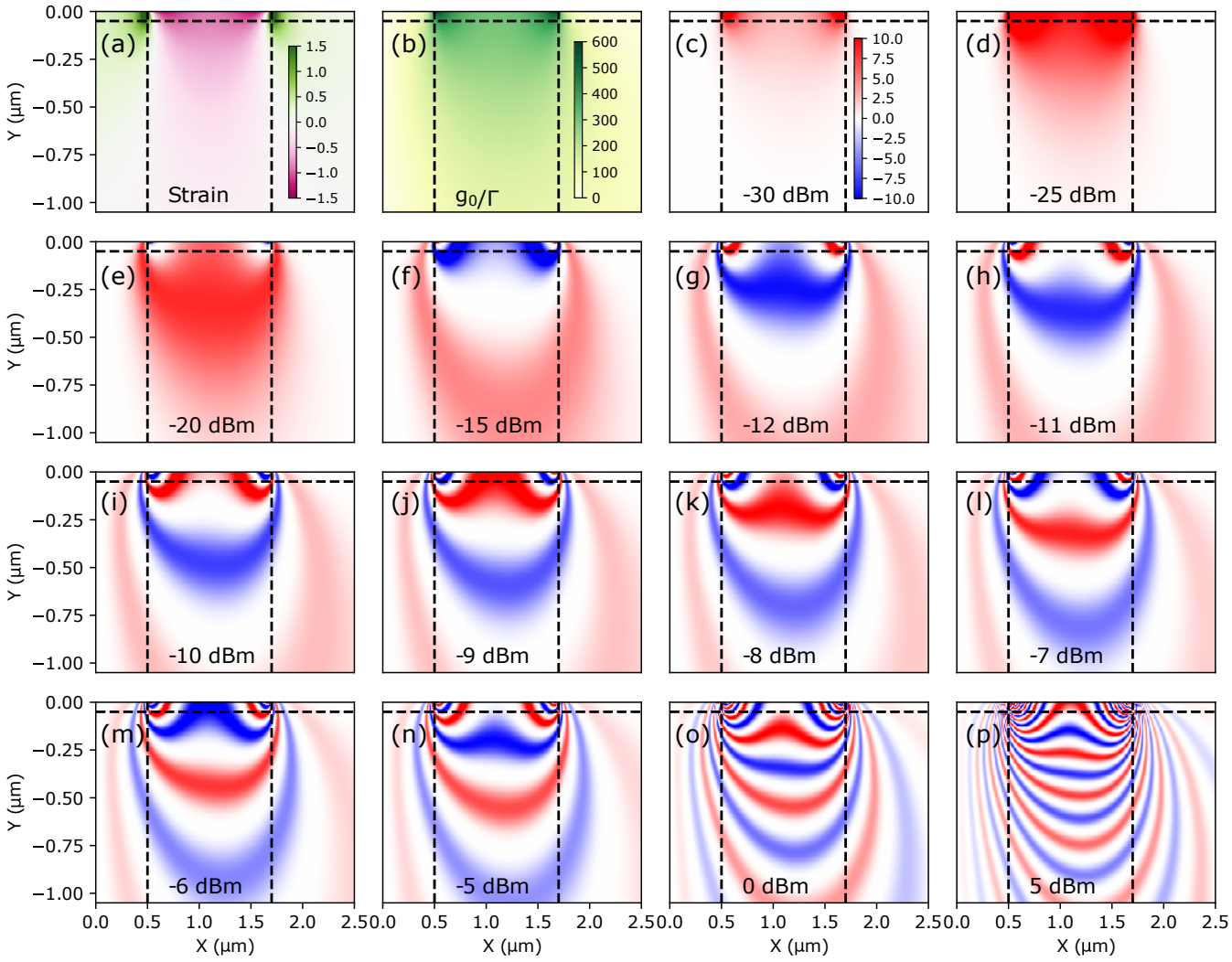


Figure S8. (a) Map of shifts in hyperfine constant (MHz) due to strain in the sample based on FE simulations as in Fig. 1(d). (b) A map of $g_0/\Gamma$ (Hz) for $S_z$ transitions, a linear rescaling of $B_1$. (c-p) maps of contribution factor for $S_z$ transitions $g_0 \sin^3(\theta(\mathbf{r}))/\Gamma$ for different pulse powers where $\theta(\mathbf{r})$ has been calculated assuming $\Gamma = 1$. In all figures the horizontal dashed line is 50 nm below the surface, approximately where electrostatic calculations imply the depletion zone, where donors are ionised due to the Schottky barrier at the Nb/Si interface [5], ends. The vertical lines are at either side of the microresonator.

linewidth

$$N_{\text{corr}} = N\frac{\kappa}{\gamma} \tag{6}$$

which yields the original term for cooperativity:

$$C_{\text{corr}} = \frac{g_0^2 N}{\kappa^2}\frac{\kappa}{\gamma} = \frac{g_0^2 N}{\kappa\gamma} \tag{7}$$

where cooperativity continues to increase with narrowing resonator linewidth, despite the fact that this reduces the number of spins within the cavity.

In general the spin ensemble lineshape is *not* identical to that of the resonator, nor is it uniformly broadened. Indeed, in these experiments the spin lineshape is asymmetric and modelled by three separate gaussian functions (six in the case of an $S_x$ transition), while the resonator is approximately Lorentzian. However this gives a good approximation and allows us to estimate the cooperativity in the narrow resonator limit in a simple manner.

Based on this, we can use the FE simulations of the resonator to estimate the ensemble coupling strength for a given distribution of spins. At each pixel the ratio of the single spin coupling, $g_0$, to the transition matrix element, $\Gamma$, is computed by $g_0/\Gamma = B_1\gamma_e$. When $B_1$ is inhomogeneous the ensemble coupling is given by $g_{\text{ens}} = \sqrt{\sum g_0^2}$ where the sum runs over spins. Voxels are defined by the 2D pixels from the simulation with out-of-page extent given by the length of the inductor (assuming that current doesn't vary significantly along the length of the inductor). Each voxel has $N_{\text{Bi}} = \rho_{\text{Bi}}(\mathbf{r})V$ bismuth atoms

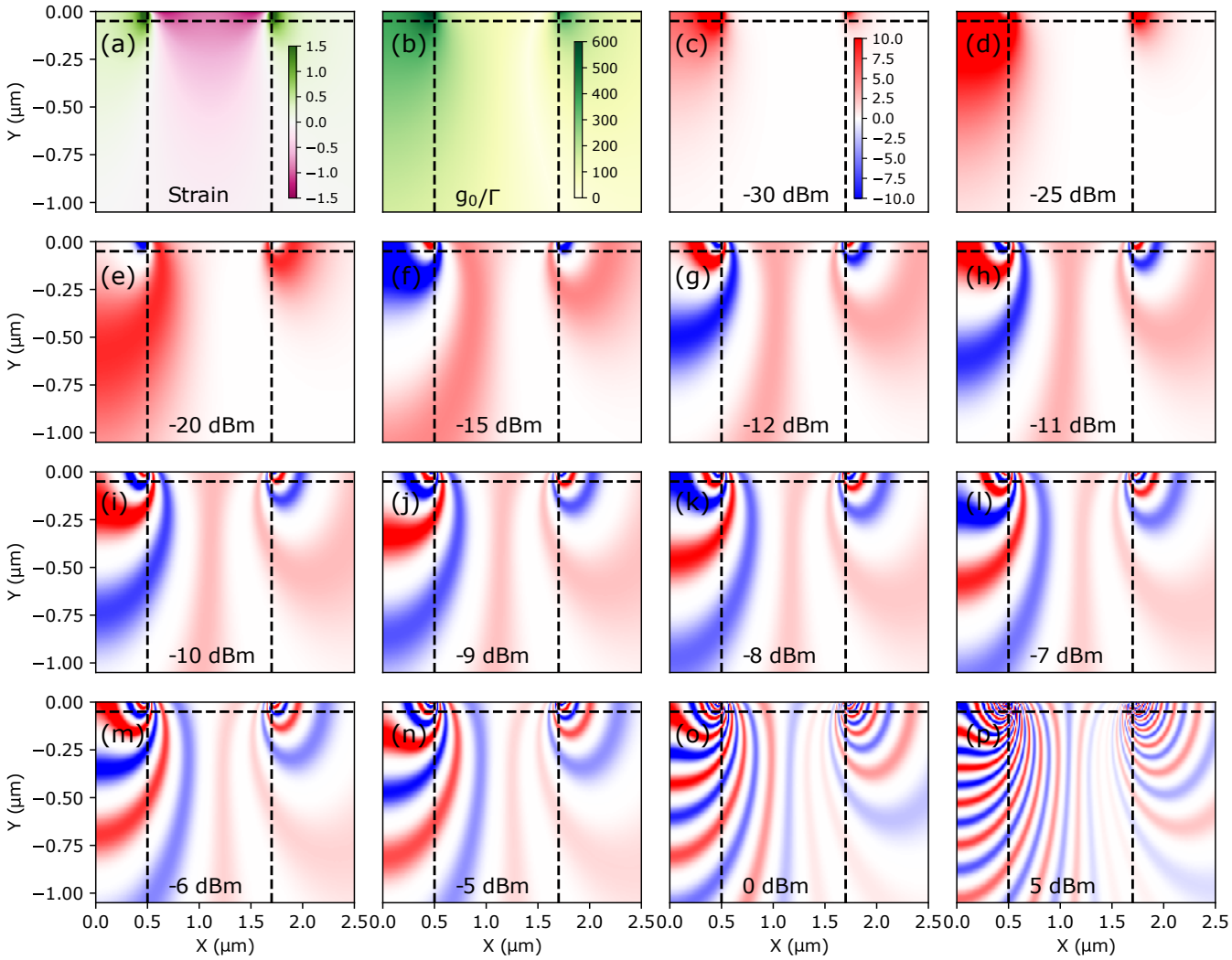


Figure S9. (a) Reproduction of S8 for $S_x$ transitions.

within it where $\rho_{\mathrm{Bi}}(\mathbf{r})$ is the local density of bismuth atoms and $V$ is the voxel volume. $N_{\mathrm{Bi}}$ is adjusted by the thermal population and then, as above, corrected so that only spins inside the cavity linewidth couple to the resonator as in Eq. 6. For the transition shown in Fig. 2 main text this computation predicts an ensemble coupling strength of ∼260 kHz, which is a factor of ∼ 2 larger than the experimental result. The discrepancy between experiment and simulation is likely due to a combination of uncertainties in the film kinetic inductance, the depletion zone depth, donor activation, a drop in current in the inductor close to the capacitive arms and spins close to the resonator having a greater linewidth and more often falling outside the cavity bandwidth. The variation in current along the inductor could be accounted for by additional simulations of the resonance mode using software packages such as CST Studio Suite.

Using these FE models we can show that continuing to add spins further from the resonator increases the coupling strength. We find that for resonators without the double-back inductor (i.e. a straight wire connecting capacitive arms) this effect is stronger as the $B_1$ fields are less confined to be local to the resonator. However, for a high fidelity memory, the spins must both add to cooperativity, and also be refocused in a quantum memory protocol. The weak $B_1$ fields means that refocusing will be inefficient and so this approach to increasing cooperativity is unsuitable if the intended application is for memories, or any application where coherent control of spins is required.

The conditions for strong coupling should also be reconsidered. As we are interested in transferring information between the resonator and spin ensemble, being able to resolve a vacuum Rabi splitting is not essential. We are interested primarily in the loss rates from the resonator and spin ensemble, and as such the regime required for quantum memories is actually $g_0\sqrt{N} \gg \kappa, \gamma_{\mathrm{h}}$.

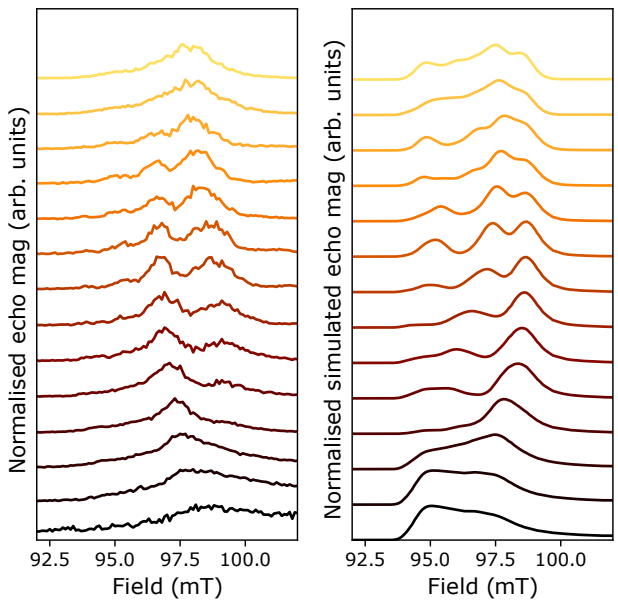


Figure S10. (a) CPMG EDFS reproduced from main text Fig. 4(g). (b) Calculated EDFS based on finite element simulations of strain and $B_1$ fields about the microresonator.

One can also define the *homogeneous cooperativity*:

$$C_{\mathrm{h}} = \frac{g_0^2 N}{\kappa \gamma_{\mathrm{h}}}. \tag{8}$$

The efficiency of the quantum memory asymptotically approaches 1 as $C_{\mathrm{h}} \to \infty$ [8]. This distinction between the homogeneous and inhomogeneous spin linewidths is why it is possible to operate an efficient quantum memory without being in the traditionally defined strong coupling regime, $g_0\sqrt{N} \gg \kappa, \gamma$. The coupling of a narrow cavity to an inhomogeneously broadened spin ensemble has also been discussed in Refs [8–11].

### G. Calculation of resonator photon number

The Rabi oscillations obtained in Fig.4 enable us to estimate the number of photons in the cavity. Using the Tavis-Cummings model for an ensemble of spins coupled to a cavity, the Rabi frequency $\Omega$ of the spins when the resonator contains $n$ photons is given by:

$$\Omega = 2g_0\sqrt{n} \tag{9}$$

We can calculate $g_0$, assuming that $T_1$ relaxation is dominated by the Purcell effect[12], using the equation:

$$\frac{1}{T_1} = \frac{4g_0^2}{\kappa} \tag{10}$$

Where $\kappa$ is the resonator half-width and $g_0$ is the resonator to single spin coupling rate. As we have seen, in this system $g_0$ varies greatly according to the position of the spins relative to the resonator and as such it is not possible to get a value for $T_1$ of the entire ensemble. We take a rough estimate of $T_1 \approx 1.5$ s to calculate $g_0 \approx 350$ Hz for spins close to the 6764 MHz resonator. We then use Eq.9 assuming $\Omega = 500$ kHz (the duration of the pre-rotation pulse used in Fig.4 was 2 µs) to calculate a photon number of $\sim 5 \times 10^5$. Note that this is only a very rough estimate and applies only to low power measurements of the spins closest to the resonator.


[1] H. Y. Carr and E. M. Purcell, Effects of diffusion on free precession in nuclear magnetic resonance experiments, Physical Review **94**, 630 (1954).

[2] S. Meiboom and D. Gill, Modified spin-echo method for measuring nuclear relaxation times, Review of Scientific Instruments **29**, 688 (1958).

[3] F. Mentink-Vigier, A. Collauto, A. Feintuch, I. Kaminker, V. Tarle, and D. Goldfarb, Increasing sensitivity of pulse epr experiments using echo train detection schemes, Journal of Magnetic Resonance **236**, 117 (2013).

[4] G. Wolfowicz, A. M. Tyryshkin, R. E. George, H. Riemann, N. V. Abrosimov, P. Becker, H.-J. Pohl, M. L. Thewalt, S. A. Lyon, and J. J. Morton, Atomic clock transitions in silicon-based spin qubits, Nature Nanotechnology **8**, 561 (2013).

[5] J. Pla, A. Bienfait, G. Pica, J. Mansir, F. Mohiyaddin, Z. Zeng, Y.-M. Niquet, A. Morello, T. Schenkel, J. Morton, and P. Bertet, Strain-induced spin-resonance shifts in silicon devices, Physical Review Applied **9**, 044014 (2018).

[6] A. Bienfait, J. Pla, Y. Kubo, M. Stern, X. Zhou, C. Lo, C. Weis, T. Schenkel, M. Thewalt, D. Vion, *et al.*, Reaching the quantum limit of sensitivity in electron spin resonance, Nature Nanotechnology **11**, 253 (2016).

[7] B. W. Maxfield and W. McLean, Superconducting penetration depth of niobium, Physical Review **139**, A1515 (1965).

[8] M. Afzelius, N. Sangouard, G. Johansson, M. Staudt, and C. Wilson, Proposal for a coherent quantum memory for propagating microwave photons, New Journal of Physics **15**, 065008 (2013).

[9] C. Grezes, Y. Kubo, B. Julsgaard, T. Umeda, J. Isoya, H. Sumiya, H. Abe, S. Onoda, T. Ohshima, K. Nakamura, I. Diniz, A. Auffeves, V. Jacques, J.-F. Roch, D. Vion, D. Esteve, K. Moelmer, and P. Bertet, Towards a spin-ensemble quantum memory for superconducting qubits, Comptes Rendus Physique **17**, 693 (2016).

[10] C. Grèzes, *Towards a Spin-Ensemble Quantum Memory for Superconducting Qubits: Design and Implementation of the Write, Read and Reset Steps* (Springer, 2015).

[11] B. Julsgaard and K. Mølmer, Reflectivity and transmis-

sivity of a cavity coupled to two-level systems: Coherence properties and the influence of phase decay, Physical Review A **85**, 013844 (2012).

[12] A. Bienfait, J. Pla, Y. Kubo, X. Zhou, M. Stern, C. Lo, C. Weis, T. Schenkel, D. Vion, D. Esteve, J. J. L. Morton, and P. Bertet, Controlling spin relaxation with a cavity, Nature **531**, 74 (2016).